Torque Ripple Minimization Control of Permanent Magnet Synchronous Motor using Adaptive Ant Colony Optimization

Ahmed Belkhadir, Driss Belkhayat, Youssef Zidani, Remus Pusca, Raphaël Romary

Ahmed Belkhadir, Driss Belkhayat, Youssef Zidani, Remus Pusca, Raphaël Romary. Torque Ripple Minimization Control of Permanent Magnet Synchronous Motor using Adaptive Ant Colony Optimization. 2022 8th International Conference on Control, Decision and Information Technologies (CoDIT), May 2022, Istanbul, Turkey. pp.629-635, 10.1109/CoDIT55151.2022.9804127 . hal-04296875

HAL Id: hal-04296875
https://univ-artois.hal.science/hal-04296875v1

Torque Ripple Minimization Control of Permanent Magnet Synchronous Motor using Adaptive Ant Colony Optimization

Ahmed Belkhadir[1,2,*], Youssef Zidani[1], Driss Belkhayat[1], Remus Pusca[2], Raphaël Romary[2]

Abstract — **Presence of fault in motor drives might cause the system to completely shutdown, reduce its performance, or cause disruptions in its operation. Therefore, having fault-tolerant capabilities to sustain continuous operation has become crucial. In this paper, the control strategy aims to minimize torque ripples and consequently vibrations under stator winding unbalance fault applied to a permanent magnet synchronous motor. The control law is based on the space phasor in order to calculate currents reference using a vector technique, allowing the fault to be corrected. Furthermore, the ACO algorithm is employed for self-tuning of controller parameters. By combining these techniques, we may improve the overall efficiency and stability of the system.**

I. INTRODUCTION

In recent years, electrical machines employed in electric mobility have shown to be the best option in terms of power density, torque/inertia ratio and high efficiency. Permanent magnet synchronous motors (PMSM) are a more appealing competitor to car manufacturers than induction motors (IM), since they have intrinsically the highest overall efficiency and a limited constant power range [1].

The behavior of an electric motor is defined by its torque-speed characteristic, which is a curve that shows the development of torque as a function of the machine's rotational speed. The torque-speed characteristic of an electric traction motor powered by a limited battery voltage is shown in "Fig. 1".

An electric vehicle's (EVs) performance is largely determined by the electric motor it uses. The traction power of the wheels is provided by the three-phase electric machine. Torque and speed are controlled by the inverter, with converts the battery's DC voltage into a three-phase AC voltage adopted to the electric machine. A bi-directional DC-DC converter ensures the transfer of energy in both directions, allowing the battery to be charged during the braking phase [2].

Torque ripples in electrical machines are due to a variety of factors and faults, including open circuits faults, lack of stator windings, inter-turn short circuit, rotor eccentricity or magnetic circuit faults. As a consequence, the reliability and safety of electrical machines has become a critical criterion for ensuring service continuity [3].

Methods for controlling and reducing torque ripples have been the subject of several studies and research. The most frequent approach involves employing estimation methods by injecting a harmonic current to the motor [4][5]. Another method recommends using a novel repeating observer methodology to minimize or decrease ripples and acoustic noise while also improving machine performance [6].

To optimize the machine's performance, a direct control strategy based on a quadratic evaluation approach and a harmonic voltage removal method is discussed and implemented in [7]. In [8][9], a reduction strategy of the impacts of faults and torque pulsations is proposed by using virtual direct quadrature axis current and direct-action voltage anticipation compensators.

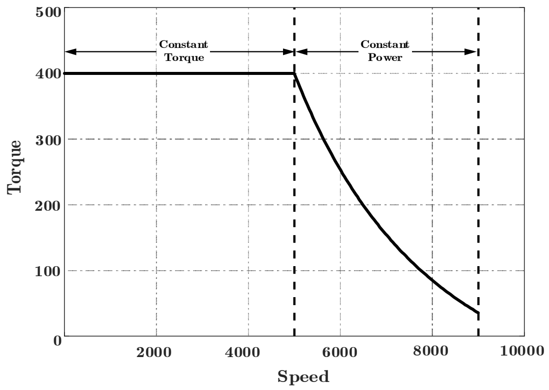

Figure 1. Torque-Speed characteristic

In this paper, a vector approach based on the current and flux space phasor is adopted to generate reference currents in order to maintain a constant torque and without ripples under the fault. These quantities are measurable or estimable, and the proposed control approach can control them. The space phasor is an interesting tool since it performs a two-axis transformation while allowing for easy reference frame switching [10]. However, the machine will be considered to be in perfect condition, with a magnetomotive force (MMF) distribution ideally rotating on the fundamental spatial plane.

The main contribution of the present paper is the development of a control strategy method able of reducing torque ripples, noise and vibrations in the case of a lack of turn on a stator phase. An enhanced fitness function that can reduce the regulator's error using an artificial Ant Colony Optimization (ACO) algorithm is provided as a robust approach for adjusting speed and current controller settings. To achieve strong stability, the cost function is reconstructed

---

[1] Laboratory of Electrical Systems Energy Efficiency and Telecommunications (LSEEET), Cadi Ayyad University, Marrakech, Morocco (email: y.zidani@uca.ma, driss.belkhayat@uca.ma).

[2] Laboratory of Electrotechnical and Environmental Systems (LSEE), Artois University, Bethune, France (email: remus.pusca@univ-artois.fr, raphael.romary@univ-artois.fr,).

*Corresponding author: (email: ahmed.belkhadir@ced.uca.ma, ahmed_belkhadir@ens.univ-artois.fr).

from two components. The suggested technique includes developing global ACO optimized PI values that are constrained to individual optimal values ISE, IAE, ITAE and ITSE.

Organization of the paper is presented as follows. Section II presents the analytical approach modeling of the PMSM. In section III, the mathematical dynamic model is described. Then, the implementation of the control law and the adaptation using ACO algorithm are detailed. Finally, the reduction of ripples is shown followed by tests and simulations results.

II. ANALYTICAL MODELLING FOR HEALTHY MACHINE

The main interest of the development is to provide generalized expressions for various quantities in a condensed form that takes into consideration all of the parameters that characterize the air gap and the machine's geometry.

A. *Air-Gap Permeance*

The analytical expression of the permeance stated in (1) is obtained by decomposing the inverse of the air-gap thickness into Fourier series, assuming that the magnetic field lines are radial.

$$\wp(\alpha^s) = P_0 + \sum_{K_s=1}^{+\infty} P_{K_s} \cos(K_s N^s \alpha^s) \tag{1}$$

$$P_0 = \frac{\mu_0}{g+p^s}\left(1+\frac{p^s+r_d^s}{g}\right) \tag{2}$$

$$P_{k_s} = 2\mu_0 \frac{p^s}{g\left(g+p^s\right)} \frac{\sin\left(K_s r_d^s \pi\right)}{K_s \pi} \tag{3}$$

Where $\mu_0 = 4\pi 10^{-7}$ is the permeability of the vaccum approximately equal to that of the air.

Any point M of the air-gap will be identified by its angular abscissa α^s in relation to the stator reference axis d^s and α^r in relation to the rotor reference d^r.

The major specifications of the PMSM are listed in Table III (Appendix), "Fig. 2" illustrates the resulting distribution of permeance in the air-gap.

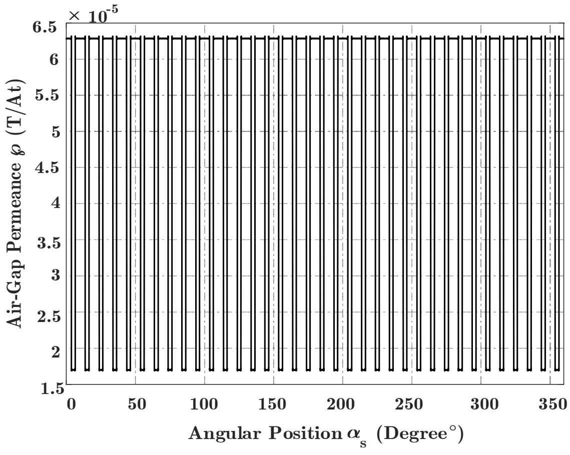

Figure 2. Air-gap permeance distribution

B. *Magnetomotive Force (MMF)*

The MMF is generated by a balanced three-phase system of currents i_q^s flowing in the stator winding. In the healthy machine, the MMF calculated relatively to the stator d^s is expressed as:

$$\varepsilon_T^s(\alpha^s) = \frac{3}{2} I^s \sum_{\substack{h_s=6j+1 \\ j=-\infty}}^{+\infty} A_{h_s}^s \cos\left[\omega t - h_s\left(p\alpha^s - \gamma^s\right)\right] \tag{4}$$

Where $A_{h_s}^s$ is a function that is dependent on the winding coefficient of the rank h_s.

The model of the evolution of the MMF produced by an elementary section is shown in "Fig. 3". This model is different from the ideal wave for a linear evolution of the MMF over the opening with of a slot. "Fig. 4" illustrates the MMF from the three-stator windings as a function of the angle α^s.

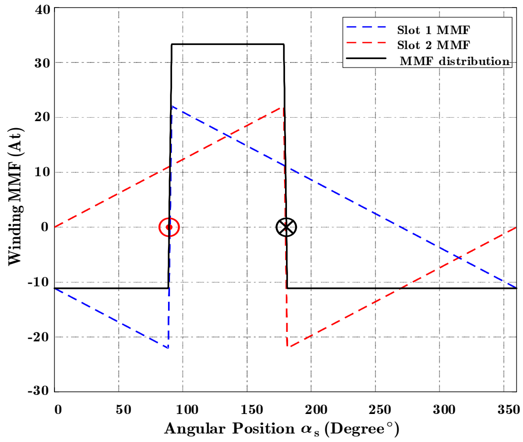

Figure 3. Winding MMF distribution into two slots

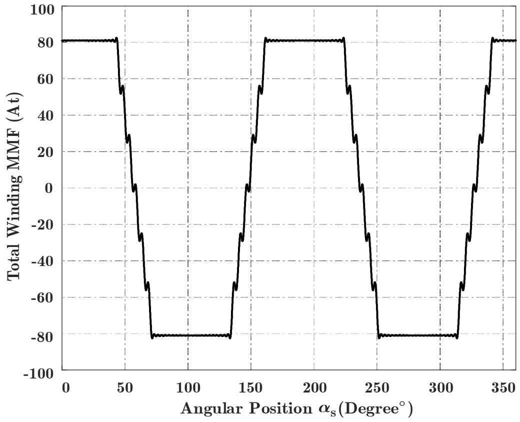

Figure 4. MMF created by healthy stator windings

C. *Air-Gap Flux Density*

The stator contribution of the air-gap flux density in the reference frame related to d^s is determined using the permeance and the MMF expressions:

$$b^s(\alpha^s) = \varepsilon_T^s(\alpha^s)\wp(\alpha^s) \tag{5}$$

The air-gap flux density time curve is shown in "Fig. 5". The waveform seems to be periodic, with fluctuations related to the slots.

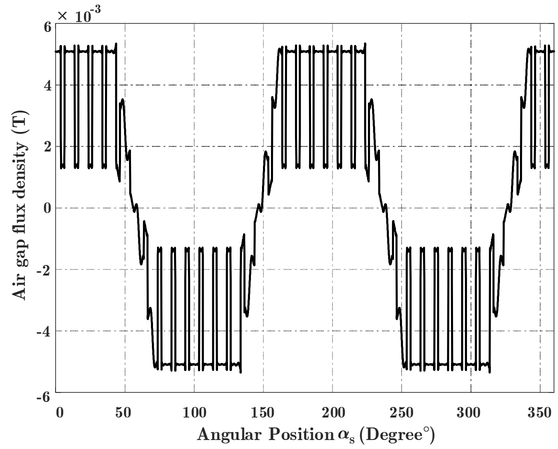

Figure 5. Air-gap flux density distribution

D. Air-Gap Field Solution

Finite Element Analysis (FEA) is the common approach for determining the air-gap field density waveform. However, even on powerful computers, it takes a long time and is difficult to include into an iterative design cycle. Alternative techniques for evaluating the air-gap field density are also recommended [11]. The standard PMSM considers a sinusoidal magnetic field distribution while neglecting the impact slots effects. Using the Conformal Mapping (CM) approach, researchers in [12] established a 2-D relative permeance function for slotting effect. [13] proposes a complex relative permeance at each position in a single slot pitch in order to anticipate the tangential component of the air-gap flux density. In the slotless air-gap, the magnetic field distribution can be represented in the present form [14][15]:

$$B_s = B_u \lambda^* = \left(B_r + jB_\theta\right)\left(\lambda_r + j\lambda_t\right)^* \tag{6}$$

The radial and tangential components of the flux density are B_r and B_θ, respectively, while the real and imaginary parts of the complex relative air-gap permeance are λ_r and λ_t. As seen below, B_r and B_θ could be expressed as a Fourier series [16]:

$$B_r\left(r,\theta\right) = \sum_{n}^{1,3,5\ldots} B_{rn}\left(r,\theta\right)\cos\left[np\left(\theta-\alpha\right)\right] \tag{7}$$

$$B_\theta\left(r,\theta\right) = \sum_{n}^{1,3,5\ldots} B_{\theta n}\left(r,\theta\right)\sin\left[np\left(\theta-\alpha\right)\right] \tag{8}$$

The Schwarz-Christoffel transformation can be used to calculate the complex air-gap permeance:

$$\lambda_r\left(r,\theta\right) = \lambda_0\left(r,\theta\right) + \sum_{m=1}^{N\lambda} \lambda_{am}(r)\cos\left(mN^s\theta\right) \tag{9}$$

$$\lambda_t\left(r,\theta\right) = \sum_{m=1}^{N\lambda} \lambda_{bm}(r)\sin\left(mN^s\theta\right) \tag{10}$$

The Fourier coefficients B_{rn} and $B_{\theta n}$ are determined by (11) and (12) respectively, based on [17]:

$$B_{rn}\left(r,\theta\right) = \sum_{n=1,3,5\ldots}^{+\infty} K_B\left(n\right) f_{Br}\left(r\right)\cos\left(np\theta\right) \tag{11}$$

$$B_{\theta n}\left(r,\theta\right) = \sum_{n=1,3,5\ldots}^{+\infty} K_B\left(n\right) f_{B\theta}\left(r\right)\sin\left(np\theta\right) \tag{12}$$

$$K_B\left(n\right) = \frac{\mu_0 M_n}{\mu_r}\frac{np}{\left(np\right)^2-1} \cdot \left\{ \frac{np-1+2\left(\frac{R_r}{R_m}\right)^{np+1} - \left(np+1\right) + \left(\frac{R_r}{R_m}\right)^{2np}}{\frac{\mu_r+1}{\mu_r}\left[1-\left(\frac{R_r}{R_s}\right)^{2np}\right] - \frac{\mu_r-1}{\mu_r}\left[\left(\frac{R_m}{R_s}\right)^{2np} - \left(\frac{R_r}{R_m}\right)^{2np}\right]} \right\} \tag{13}$$

$$f_{Br}(r) = \left(\frac{r}{R_s}\right)^{np-1}\left(\frac{R_m}{R_s}\right)^{np+1}\left(\frac{R_m}{r}\right)^{np+1} \tag{14}$$

$$f_{B\theta}(r) = -\left(\frac{r}{R_s}\right)^{np-1}\left(\frac{R_m}{R_s}\right)^{np+1}\left(\frac{R_m}{r}\right)^{np+1} \tag{15}$$

“Fig. 6” and “Fig. 7” illustrates the radial and tangential components of complex relative permeance in the center of the air-gap without considering magnetic saturation. As shown, the unsaturated complex relative air-gap permeance is relatively comparable across all slot pitches that can be calculated using Fourier series. “Fig. 8” shows examples of the field solution in the middle of the air-gap. As can be seen, the flux density of the PMSM employed in (EVs) is not perfect sinusoidal.

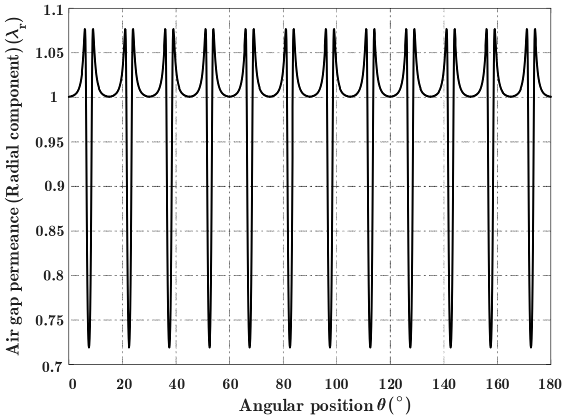

Figure 6. Radial component of air-gap complex permeance

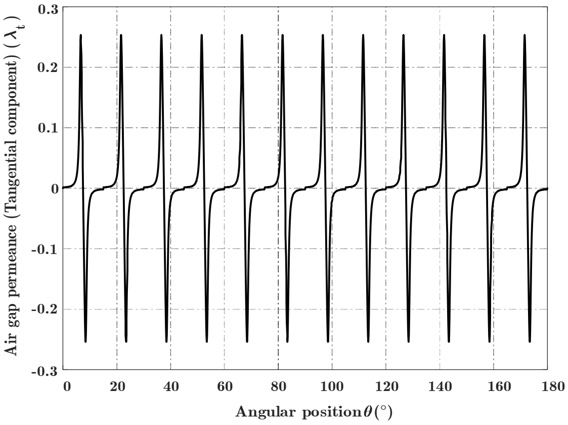

Figure 7. Tangential component of air-gap complex permeance

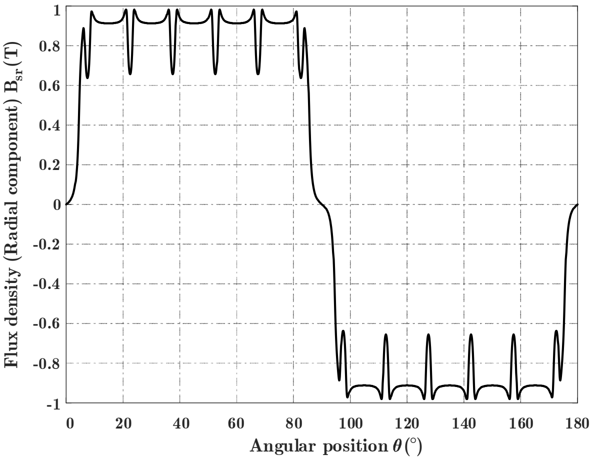

Figure 8. Radial component of the flux density

III. PMSM MODEL

It is simple to implement the lack of turns fault using the abc reference model. To eliminate torque ripples, the abc model is utilized to estimate the effect of the fault using the control technique. Three-phase PMSM's well-known voltage expression is as follows:

$$\left[V_{s,abc}\right]=\left[r_{s,abc}\right]\left[i_{s,abc}\right]+\left[L_{abc}\right]\frac{d}{dt}\left[i_{s,abc}\right]+\frac{d}{dt}\left[\phi_{r,abc}\right] \tag{16}$$

In the presence of the fault, the neutral point's potential can be changed. As a result, we use the voltage equations without V_n:

$$\begin{cases}\dfrac{d}{dt}\phi_a-\dfrac{d}{dt}\phi_b=V_a-V_b-r_ai_a+r_bi_b\\ \dfrac{d}{dt}\phi_b-\dfrac{d}{dt}\phi_c=V_a-V_c-\left(r_a+r_c\right)i_a-r_ci_b\end{cases} \tag{17}$$

$$i_a=\frac{\left(\phi_a-\phi_{ra}-\phi_b+\phi_{rb}\right)-\left(M_{ab}-M_{ac}-L_{bb}+M_{bc}\right)i_b}{L_{aa}-M_{ac}-M_{ba}+M_{bc}} \tag{18}$$

$$i_b=\frac{\left(\phi_a-\phi_{ra}-\phi_c+\phi_{rc}\right)-\left(L_{aa}-M_{ac}-M_{ca}+L_{cc}\right)i_a}{M_{ab}-M_{ac}-M_{cb}+L_{cc}} \tag{19}$$

The product of the flux's space vector and the currents yields the following expression for electromagnetic torque:

$$\Gamma_e=\frac{3}{2}p\left(\bar{\phi}_s\wedge\bar{i}_s\right) \tag{20}$$

The space phasor of current and the flux can be obtained with:

$$\bar{i}_s=\frac{2}{3}\left(i_a+i_ba+i_ca^2\right) \tag{21}$$

$$\bar{\phi}_s=\frac{2}{3}\left(\phi_a+\phi_ba+\phi_ca^2\right) \tag{22}$$

Where $a=e^{j(2\pi/3)}$

IV. TORQUE RIPPLE REDUCTION CONTROL STRATEGY

A. The Implementation of the Control Technique

In the case of our study, the primary part of the control strategy is to eliminate the ripples using current control. According to the torque equation (20), which is generated from a vector product between the flux and current. However, in order to get maximum torque, the current and flux must be in quadrature. As a result, the control law must follow a constant and maximum torque, implying that the flux is in quadrature with the current.

$$\Gamma_e^*=\frac{3}{2}p\left(\phi_di_q^*-\phi_qi_d^*\right)=cste \tag{23}$$

$$i_d^*=-\frac{\phi_qi_q^*}{\phi_d} \tag{24}$$

$$i_q^*=-\frac{\phi_di_d^*}{\phi_q} \tag{25}$$

By replacing equations (24) and (25) in equation (23), the reference currents giving a constant torque without ripples are obtained:

$$\begin{cases}i_d^*=-\dfrac{2}{3p}\Gamma_e^*\dfrac{\phi_q}{\phi_d^2+\phi_q^2}\\ i_q^*=\dfrac{2}{3p}\Gamma_e^*\dfrac{\phi_d}{\phi_d^2+\phi_q^2}\end{cases} \tag{26}$$

Taking into account the real and imaginary elements of the space phasor of the flux:

$$\begin{cases}\phi_d=\Re\left(\bar{\phi}_s\right)\\ \phi_q=\Im\left(\bar{\phi}_s\right)\end{cases} \tag{27}$$

The space vector of the reference current is expressed in terms of its real and imaginary parts:

$$\bar{i}_s^*=i_d^*+ji_q^* \tag{28}$$

The reference currents are given by the following equations:

$$\begin{cases}i_a^*=\Re\left(\bar{i}_s^*\right)\\ i_b^*=\Re\left(a\bar{i}_s^*\right)\\ i_c^*=\Re\left(a^2\bar{i}_s^*\right)\end{cases} \tag{29}$$

B. Parameter Adaptation Using ACO Algorithm

In order to achieve the best value for the control parameters, ACO algorithm is used. To operate the algorithm-based tuning procedure, commonly used error criteria are used to obtain an optimum controller are Integral Square Error (ISE), Integral Absolute Error (IAE), Integrated Time Absolute Error (ITAE) and Integral Time Square Error (ITSE), respectively, and are expressed as given in (30), (31), (32) and (33), respectively.

$$ISE=\int\left[e\left(t\right)\right]^2dt \tag{30}$$

$$IAE = \int \left| e(t) \right| dt \quad (31)$$

$$ITAE = \int t \left| e(t) \right| dt \quad (32)$$

$$ITSE = \int t \left[e(t) \right]^2 dt \quad (33)$$

The ACO algorithm is inspired on the comportment of ants. It is a technique for resolving optimization issues. This method is a revolutionary heuristic bionic algorithm based on the behavior of ants foraging for food in the nature [18]. The design PI issue is shown in “Fig. 9” using the ACO algorithm, also the diagram that explains the steps of the algorithm. Table I summarizes the parameters of the program.

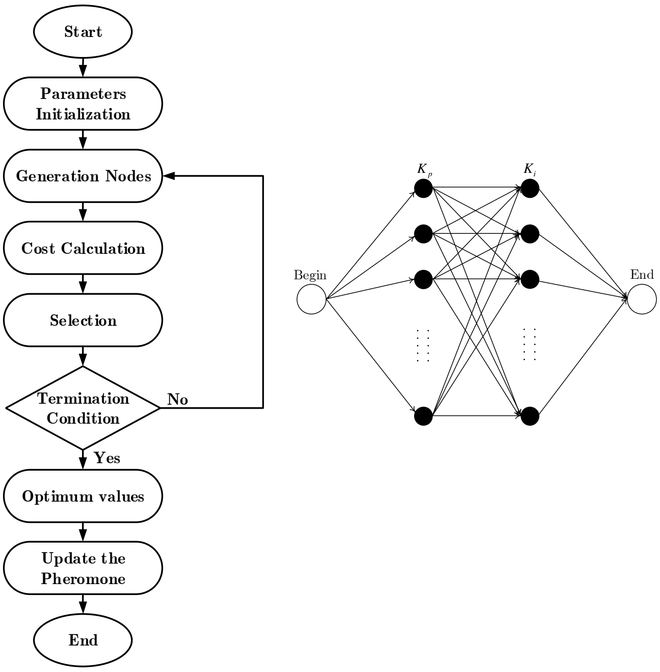

Figure 9. Flow chart of ACO algorithm

TABLE I. ACO PARAMETERS

Parameter	Value
Number of parameters	4
Number of ants	50
Maximum number of iteration	70
Number of nodes	1000
Pheromone evaporation rate	0

To summarize, “Fig. 10” depicts the structure of the control loop used to remove torque ripples. The reference currents are determined from a reference torque provided by the speed loop and the flux’s space phasor. To assess the performance and quantify the ripples, the currents will be measured.

V. SIMULATION RESULTS

MATLAB/Simulink is used to verify the proposed structure. The following simulations are carried out under one level of fault (A lack of turns of 25% of the elementary section). The parameters are taken into consideration by an 8 s step change from the healthy to the faulty case. The angle between the current and the electromotive force is 90°, resulting a maximum torque. To assess performance and quantify the impact of the fault on torque ripples, the three-phase current, torque and speed delivered by the PMSM will be evaluated. Experimental validation employing sensors to analyze the magnetic field of dispersion may identify this type of fault. The benefit of this technology in terms of diagnosis is that it is non-invasive, which means that it will not disrupt normal operations due to an on-line implementation.

“Fig. 11” illustrates the evolution of the electromagnetic torque. At 8 s, the torque presents high ripples, which correspond to the double of the supply frequency. “Fig. 12” present the motor speed in the presence of fault, which causes vibrations and acoustic noise due to intolerable speed ripples. This can be explained by a decrease in one phase’s resistance and inductance, which increases the system’s pass-band. Therefore, including a control strategy will be essential. In correlation with the torque ripples, the current (“Fig. 13) absorbed by the motor exhibit a bigger variation during the faulty state. This is due to the decrease of the machine’s capacity to generate torque by the decrease of the flux generated by the rotor in the stator winding.

Due to the obvious high levels of static error and ripples, the controllers must be optimized using the ACO algorithm according to the machine’s operating mode.

The ability to operate in the presence of the fault is crucial in the application of EVs. In order to minimize ripples and prevent fault propagation, the validity of the structure and the adopted algorithm must be verified (“Fig. 10”). The simulations present the machine’s variations using the space phasor. This control will generate an unbalanced current system to compensate the negative effects introduced by the fault.

According to the analysis of electromagnetic torque variation, fluctuations and ripples in fault-tolerant operation appear to be stable (“Fig. 14”). As a result, it can be concluded that the suggested structure can successfully maintain the motor running continuously when the fault arises. “Fig. 15” depicts the evolution of the PMSM speed in the case of fault with correction strategy. It is obvious that the motor is able to run correctly. In addition, the response and the rise time of the transient state were lowered. As a result, good performance indices. “Fig. 16” describe the simulation results of the three-phase current. The proposed structure is able to eliminate the effect of fault and ripples in the fault-tolerant condition.

As can be seen in “Fig. 17”, the response signal ITSE drops quicker, the convergence velocity of ITSE is clearly the best when compared to other approaches. It is worth nothing that the ITAE provides good results, although its response time is not the greatest. However, the integral time square error (ITSE) is the optimum option. The parameters of the controllers are presented in Table IV (Appendix).

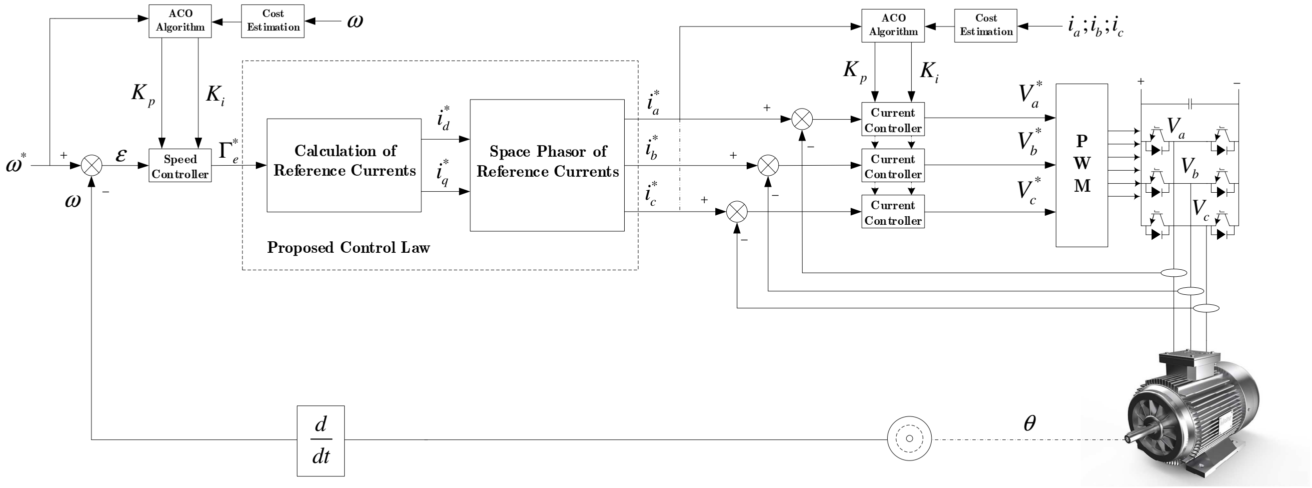

Figure 10. Block diagram of the proposed strategy

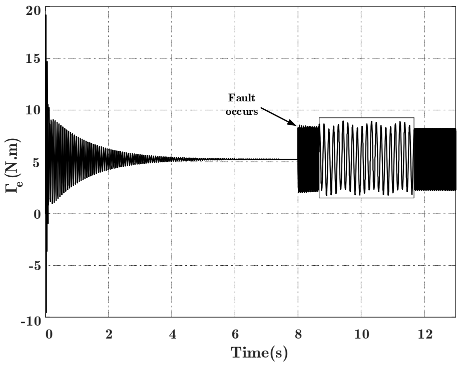

Figure 11. Electromagnetic torque during the fault

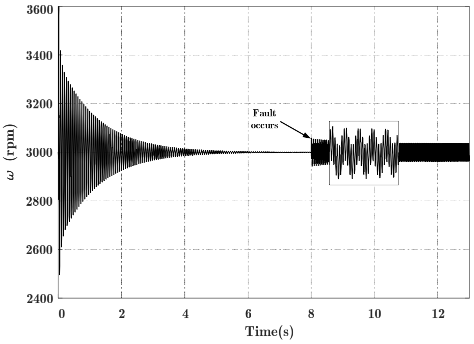

Figure 12. Rotor speed during the fault

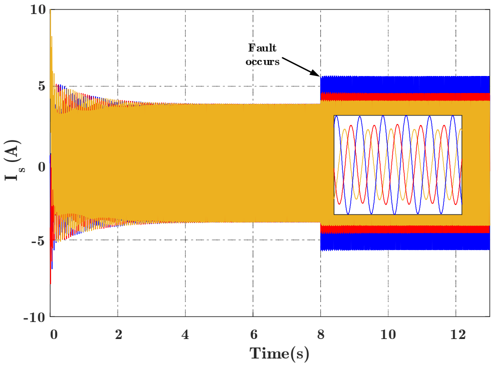

Figure 13. Stator currents during the fault

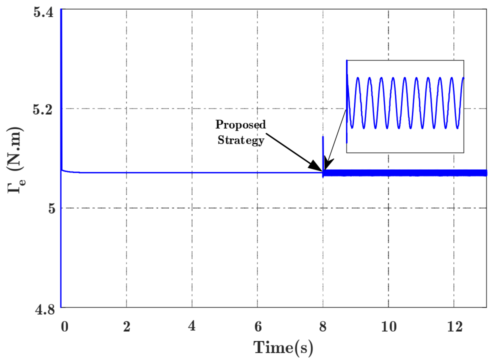

Figure 14. Electromagnetic torque after correction approach

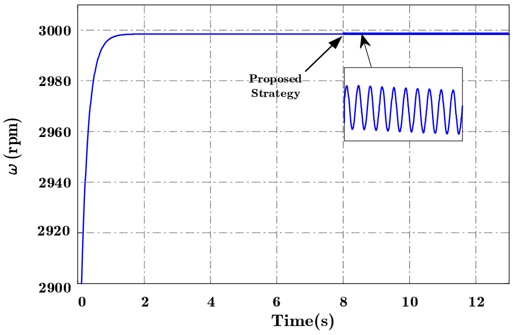

Figure 15. Rotor speed after correction approach

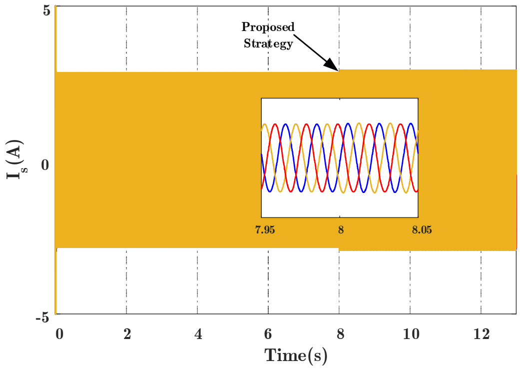

Figure 16. Stator currents after correction approach

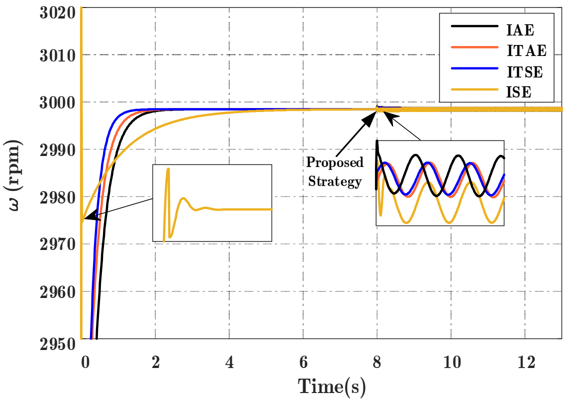

Figure 17. Comparison of speed using errors criterion

The results obtained are shown in Table II. We noticed that the level of the torque ripples is proportional to the fault level. Current and speed ripples increase. The control strategy leads to minimize ripples.

TABLE II. SUMMARY OF SIMULATION RESULTS

	Healthy	**Faulty state without correction**	**Faulty state with correction**
$\Gamma_e(N.m)$	5.264	[2.312;8.230]	[5.202;5.306]
$i_{a,\max}(A)$	3.83	5.635	2.439
$i_{b,\max}(A)$	3.83	4.625	2.438
$i_{c,\max}(A)$	3.83	4.115	2.434
ε_a	-	-	0.1
ε_b	-	-	0.1
ε_c	-	-	0.1
$\omega_e(rpm)$	3000	[2942;3056]	[2998.7;2999.8]
ε_{ω_e}	-	-	0.0323

VI. CONCLUSION

The aim of this paper is to assess the efficiency of the improved structure in eliminating ripples and decreasing PMSM's unacceptable acoustic noise under stator winding fault situations. ACO algorithm is used to estimate speed and currents controller parameters, and it has proven to be a powerful tool for solving optimization issues. The suggested strategy was based on the space phasor by injecting an unbalanced three-phase system of current, enabling reducing the pulsations and impacts of fault.

This paper evaluated the suggested method's feasibility. Future work includes: experimentally implement the control law to reduce ripples; highlight the possibility of formalizing the combination between diagnosis and fault-tolerant control; development more accurate strategy in order to eliminate ripples under faults; and testing the implementations and test at higher motor speeds for real EVs applications.

APPENDIX

TABLE III. PMSM PARAMETERS

Parameter	**Symbol**	**Value**	**Unit**
Stator resistances	r_a,r_b,r_c	2.5	Ω
Stator inductances	L_{aa},L_{bb},L_{cc}	82.4	mH
Mutual inductances	M_{ab},M_{bc},M_{ac}	-41.2	mH
Total inertia	J	0.0024	Kg.m^2
Friction	F	0.008	Nm.s.rd^{-1}
Pole pairs number	p	2	-
Slot number	N^s	36	-
Stator fictive slot depth	p^s	0.054	cm
Air-gap length	g	0.5	mm
Stator slot width	l_e^s	0.27	cm
Stator tooth width	l_d^s	0.73	cm
Radius of the rotor surface	R_r	55	mm
Radius of the magnet surface	R_m	57	mm
Radius of the stator surface	R_s	57.5	mm
Magnet remanence	B_r	1.2	T

TABLE IV. OPTIMAL VALUES OF ACO

Cost function	**K_p**	**K_i**
ISE	$K_{p_{speed}}=3.2881$	$K_{i_{speed}}=2.9056$
	$K_{p_{current}}=408.1081$	$K_{i_{current}}=624.9249$
IAE	$K_{p_{speed}}=0.74254$	$K_{i_{speed}}=2.2728$
	$K_{p_{current}}=1465.5656$	$K_{i_{current}}=212.2122$
ITAE	$K_{p_{speed}}=0.958335$	$K_{i_{speed}}=3.28328$
	$K_{p_{current}}=1613.9139$	$K_{i_{current}}=444.2442$
ITSE	$K_{p_{speed}}=0.74744$	$K_{i_{speed}}=3.45005$
	$K_{p_{current}}=1851.654$	$K_{i_{current}}=282.5825$

REFERENCES

[1] N. Hashernnia & B. Asaei B. "Comparative Study of Using Different Electric Motors in the Electric Vehicles". *Proceedings of the 2008 International Conference on Electrical Machines*. doi: 10.1109/icelmach.2008.4800157

[2] Erik Schaltz. "Electrical Vehicle Design and Modeling". *Intechopen, September 12th 2011*. doi: 10.5772/20271

[3] I. Sadeghi, H. Ehya , J. Faiz, & A. A. S. Akmal. "Online Condition Monitoring of Large Synchronous Generator under Short Circuit Fault-A Review". *IEEE Conference on Industrial Technology (ICIT)*, 2018, pp. 1843-1848. doi: 10.1109/icit.2018.8352465

[4] H. Liu, D. Wang, X. Yi, & F. Meng. "Torque Ripple Suppression under Open-Phase Fault Conditions in a Five-Phase Induction Motor with Harmonic Injection". 2019 *IEEE Journal of Emerging and Selected Topics in Power Electronics*

[5] S. H. Park, J. C. Park, S. W. Hwang, J. H. Kim, H. J. Park & M. S. Lim. "Suppression of Torque Ripple Caused by Misalignment of the Gearbox by using Harmonic Current Injection Method". 2020 *IEEE/ASME Transactions on Mechatronics*

[6] M. Tang, S. Odhano, A. Formentini & P. Zanchetta. “Reuse of a and Acoustic Noise Elimination using a Novel Repetitive Observer”. 2019 *IEEE Energy Conversion Congress and Exposition*

[7] G. Li, J. Hu, Y. Li & J. Zhu. “An Improved Model Predictive Direct Torque Control Strategy for Reducing Harmonic Currents and Torque Ripples of Five Phase Permanent Magnet Synchronous Motors”. 2018 *IEEE Transactions on Industrial Electronics*.

[8] R. Cui, Y. Fan & C. Li. “On-line Inter-turn Short-circuit Fault Diagnosis and Torque Ripple Minimization Control Strategy Based on OW Five-phase BFTHE-IPM”. 2018 *IEEE Transactions on Energy Conversion*. doi:10.1109/tec.2018.2851615

[9] Y. Guo, L. Wu, X. Huang, Y. Fang & J. Liu. “Adaptive Torque Ripple Suppression Methods of Three-Phase PMSM During Single-Phase Open-Circuit Fault-Tolerant Operation”. 2020 *IEEE Transactions on Industry Applications*. doi: 10.1109/tia.2020.3004305

[10] A. ZUCKERBERGER & A. ALEXANDROVITZ. “Space-Phasor Model of a Three-Phase Induction Motor with a View to Digital Simulation”. Vol 12, 1987 *Electric Power Systems Research*.

[11] X. Chen, J. Hu, K. Chen & Z. Peng. “Modeling of electromagnetic torque considering saturation and magnetic field harmonics in permanent magnet synchronous motor for HEV”. 2016 *Simulation Modelling Practice and Theory*, pp. 212-225

[12] Z. Q. Zhu & D. Howe. “Instantaneous Magnetic Field Distribution in Brushless Permanent Magnet dc Motors, Part III: Effect of Stator Slotting”. 1993 *IEEE Transactions on Magnetics*, vol. 29, pp. 143-151. doi: 10.1109/20.195559

Damaged Permanent Magnet Synchronous Motor for Torque Ripple

[13] D. Zarko, D. Ban & T. A. Lipo. “Analytical Calculation of Magnetic Field Distribution in the Slotted Air Gap of a Surface Permanent-Magnet Motor Using Complex Relative Air-Gap Permeance”. 2006 *IEEE Transactions on Magnetics*, vol. 42, 1828-1837. doi: 10.1109/tmag.2006.874594

[14] D. Zarko, D. Ban & T. A. Lipo. “Analytical Solution for Electromagnetic Torque in Surface Permanent-Magnet Motors Using Conformal Mapping”. 2009 *IEEE Transactions on Magnetics*, vol. 45, pp. 2943-2954. doi: 10.1109/tmag.2009.2014689

[15] F. R. Alam & K. Abbaszadeh. “Magnetic Field Analysis in Eccentric Surface-Mounted Permanent-Magnet Motors Using an Improved Conformal Mapping Method”. 2016 *IEEE Transactions on Energy Conversion*, pp. 333-344. doi: 10.1109/tec.2015.2479562

[16] D. Zarko, D. Ban & T. A. Lipo. “Analytical Solution for Cogging Torque in Surface Permanent-Magnet Motors Using Conformal Mapping”. 2008 *IEEE Transactions on Magnetics*, vol. 44, pp. 52-65. doi: 10.1109/TMAG.2007.908652

[17] Z. Q. Zhu, D. Howe & C. C. Chan. “Improved Analytical Model for Predicting the Magnetic Field Distribution in Brushless Permanent-Magnet Machines”. 2002 *IEEE Transactions on Magnetics*, vol. 38, pp. 229-238. doi: 10.1109/20.990112

[18] S. Fidanova. “Ant Colony Optimization and Applications”. 2021 *Studies in Computational Intelligence,* vol. 947. doi : 10.1007/978-3-030-67380-2